Geoscience Letters

RESEARCH LETTER

Open Access

Interplay of greening and ENSO on biosphere–atmosphere processes in Australia

Shijing Liang[1], Alan D. Ziegler[2], Laurent Z. X. Li[3], Jie Wu[1,4], Dashan Wang[1] and Zhenzhong Zeng[1*]

Abstract

Terrestrial ecosystems are fully coupled with the climate. The planet has been greening owing to the increased vegetation growth in response to the changing atmosphere, which in turn has feedback on the climate. Greening has slowed down the rise in global land-surface air temperature mainly through a coincident increase of evapotranspiration and precipitation in wet regions. In dry regions, greening intensifies the decrease in soil moisture induced by greening-enhanced transpiration. Uncertain, however, is how the climate effects of greening in semi-arid lands might differ for variable wet and dry conditions. Here, we focus on the biosphere–atmosphere interactions in Australia by modeling the perturbation of vegetation changes under various states of sea surface temperature (SST), including the climatology mean, El Niño, and La Niña conditions. For the dry conditions of El Niño, greening exacerbates water stress and largely depletes the soil moisture, while for the wet conditions of La Niña, greening-enhanced evapotranspiration and precipitation resupply the soil moisture. For the normal conditions using the climatology mean SST, a small decrease in soil moisture occurs but with large spatial contrast because of heterogeneous changes of evapotranspiration and precipitation induced by greening. We emphasize that the alternating dry and wet conditions modulated by the large-scale climate variability are vital to understanding the response of climate to greening. Furthermore, vegetation-based warming mitigation policies need to be cautious when inferring distinct climate effects associated with greening.

Keywords: Leaf Area Index, Earth system model, Evapotranspiration, Soil moisture, Atmospheric circulation, Climatology

Introduction

As much as one-quarter to one-half of the land surfaces globally may have experienced greening, which is not uniformly distributed worldwide as it is limited by water and nutrient availability (Piao et al. 2020). Enhanced vegetation growth has been observed since the 1980s, known as earth greening (Liu et al. 2010; Zhu et al. 2016). Greening imposes changes on biosphere–atmosphere interactions, affecting global hydrometeorological processes and the climate (Zeng et al. 2018a; Piao et al. 2020). Typically represented as the increase in Leaf Area Index (LAI), greening enhances evaporative cooling on land owing to the increased efficiency of water vapor transfer to the atmosphere (Chen et al. 2020). Greening also reduces albedo inducing a warming effect (Thompson et al. 2022). Consequentially, greening potentially provides negative forcing that counters greenhouse gases-driven warming (Forzieri et al. 2017; Zeng et al. 2018b). Meanwhile, increased evapotranspiration (ET) related to greening tends to reduce soil moisture and intensify the global terrestrial hydrological cycle (Feng et al. 2021).

At subcontinental scales, the effect of greening on biosphere–atmosphere processes produces highly

*Correspondence: zengzz@sustech.edu.cn

[1] School of Environmental Science and Engineering, Southern University of Science and Technology, Shenzhen, China
Full list of author information is available at the end of the article

heterogeneous patterns of precipitation. In Amazonia, a recognized wet-climate greening hotspot (Spracklen et al. 2012; Chen et al. 2019), enhanced ET supplies water vapor to the atmosphere, thereby potentially increasing precipitation via a process known as moisture recycling. Simply, moisture recycling refers to local ET returning moisture into the atmosphere which in turn becomes precipitation (Trenberth 1999). Greening-enhanced precipitation may then recharge soil wetness, balancing the losses in soil moisture triggered by the enhanced ET (Li et al. 2018; van der Ent et al. 2010). In contrast, many arid and semi-arid regions have experienced decreasing trends in soil moisture over the past two decades that correspond with the greening effect (Deng et al. 2020). To date, limited work has addressed the biosphere–atmosphere interactions in arid and semi-arid regions where wetness conditions may vary greatly in response to synoptic-scale meteorological forcing.

The Australian continent is an ideal location for investigating the interplay of greening and biosphere–atmosphere interactions. The relatively small human interference and the isolation of the continent allow the vegetation to respond naturally to distinct fluctuating periods of ample and insufficient rainfall (Jiao et al. 2021). From the early 1980s to the 2010s, greening in Australia has increased vegetation cover by 9.3% (Additional file 1: Table S1). Similarly, Winkler et al. (2021) report a 3.84% per decade (1982–2017) increase in LAI for Australian shrublands (cf. Poulter et al. 2014). Earlier, Donohue et al (2009) reported observable greening of nearly 8% during 1981–2006 across Australia. Enhanced vegetation growth mainly occurred in the northern, southern, and eastern regions of Australia—among a variety of climate regimes where annual precipitation ranges widely from less than 300 mm to more than 1500 mm (Fig. 1). CO_2 fertilization is assumed to be the dominant factor driving the greening, which overlaps spatially with many large agriculture areas in Australia (Zhu et al. 2016; Piao et al. 2020; Chen et al. 2019). For example, the Murray-Darling Basin in the southeast region is a recognized greening hotspot (Chen et al. 2019). The dry interior of Australia is particularly relevant to this discussion because greening may affect the naturally evolved ability of various arid and semi-arid biomes to persist despite substantial climate variability (Hill et al. 2006; Jiao et al. 2021).

In Australia as a whole, alternating wet and dry conditions are mainly caused by variable weather systems affected by coupled oceanic and atmospheric phenomena. El Niño and Southern Oscillation (ENSO), for example, is one dominant system driving precipitation variability in Australia (Liguori et al. 2022). ENSO is typically identified by varying warm and cold SST patterns in the Pacific Ocean (Liguori et al. 2022; Risbey et al. 2011).

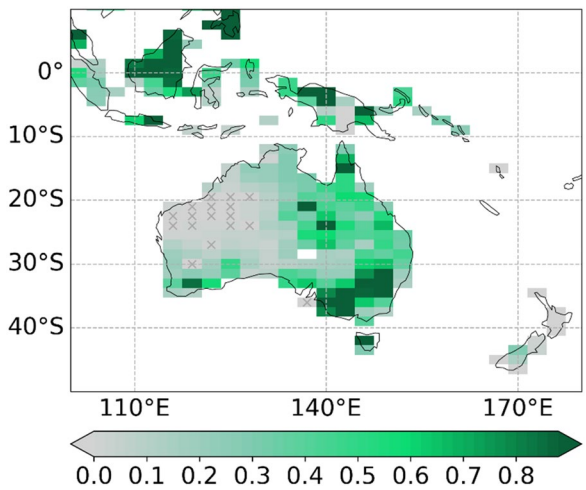

Fig. 1 Observed change in LAI. The spatial pattern of greening is calculated as the difference between the mean LAI in the periods 2007–2011 and 1982–1986. The greening pattern is interpolated to be consistent with the resolution of the model input. The cross symbols show pixels where LAI changes are small (< 10th percentile)

During La Niña, western Pacific waters are particularly warm, promoting convection; during El Niño, the warming shifts to the eastern Pacific Ocean, reducing convection in the vicinity of Australia where SSTs have cooled (Fig. 2e, f). A prior modeling study found that with a fixed mean SST, greening triggered a warm and dry trend in Australia from 1982 to 2011 (Zeng et al. 2017). Characteristics of this trend were reductions in soil moisture, suppressed ET, and intensified water stress (Wu et al. 2022). The model-based findings are consistent with those of an observation-based study (Deng et al. 2020). However, when considering year-to-year SST variations, greening produced an opposite wet and cooling trend (Zeng et al. 2017). Such contrasting impacts are believed to be associated with the influence of SST variation on ocean–atmosphere circulations that influence moisture transport pathways from the ocean, affecting precipitation patterns inland (Yu et al. 2017; Li et al. 2018). Collectively, the results of prior studies showing that altering wet and dry conditions in Australia are closely associated with SST extremes suggest that ENSO affects the influence of greening on biosphere–atmosphere interactions in Australia.

Regional studies in Australia elaborate on the climate impacts of greening. For example, observation-based studies link LAI trends with changes in ecohydrological variables (e.g., soil moisture, precipitation, and ET) and emphasize the role of greening in exerting changes in water availability (Hutley et al. 2001; Ellis and Hatton 2008; Chen et al. 2014). However, works based on statistical analyses struggle to isolate the mechanisms

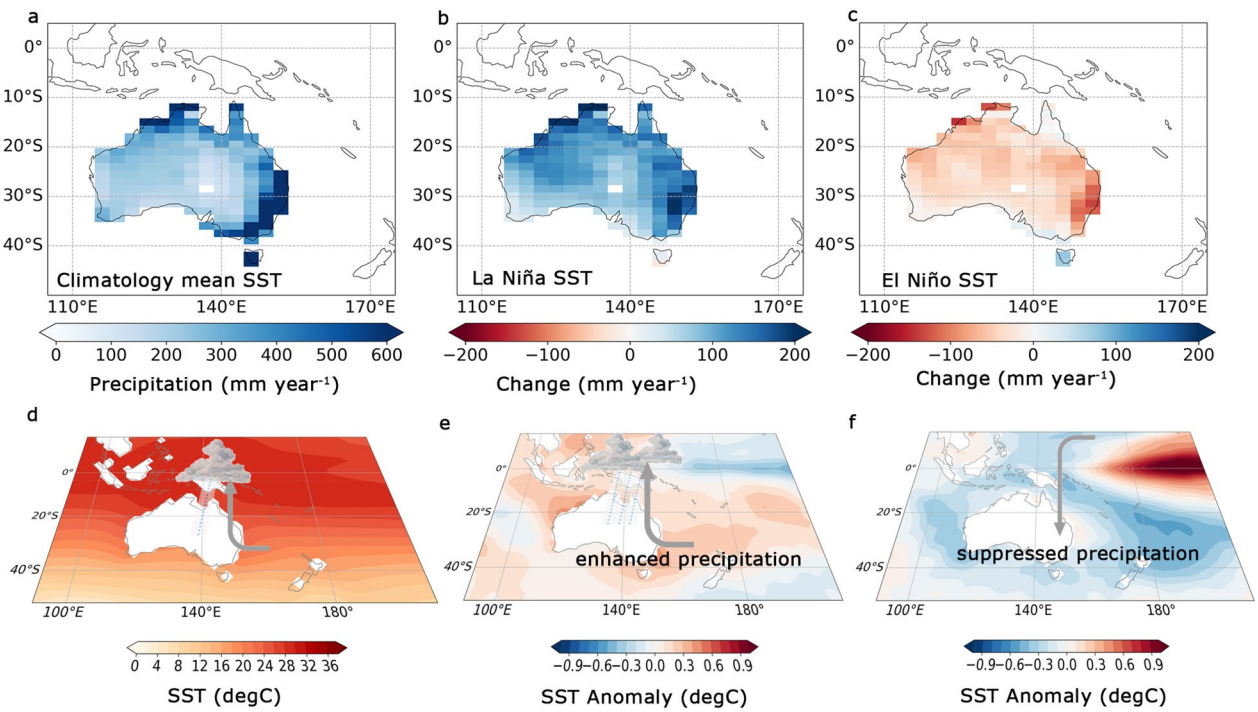

Fig. 2 Changes in precipitation under different SSTs. **a** The mean annual precipitation under the climatology mean SST condition. **b**, **c** Changes in mean annual precipitation for La Niña and El Niño SST forcing conditions extracted by the pattern of the climatology mean SST, respectively. **d**–**f** The conceptual illustrations of precipitation associated with different SST forcings. **d** Convection from the western Pacific (east of Australia) contributes to the precipitation on the continent. **e** Anomalous warm SST tends to enhance more precipitation in Australia. The SST anomaly is computed as the La Niña mean SST minus the climatology mean SST. **f** The anomalous cold SST under the El Niño condition suppresses the precipitation in Australia

by which greening affects the ecohydrological processes (Donohue et al. 2009). The modeling study of Chen et al. (2014) regarding climate variability and vegetation water use showed the ability of savanna vegetation to greatly reduce water recharge in the soil in dry years. However, the simulation approach neglected the influence of the ocean, thereby reducing the utility of the findings to informing on biosphere–atmosphere interactions (Chen et al. 2014). Another modeling study on vegetation feedback on the Asian-Australian Monsoon determined that greening tends to enhance ET and increase precipitation in Australia (Notaro et al. 2017). Though these studies are informative, the previous conclusions on the climate impacts of greening remain insufficient as they did not consider the interplay between the hydrological feedback and the SST variations, for example, as influenced by ENSO.

In addressing these research gaps, we perform diagnostic simulations using coupled land–atmosphere global climate model from the Institute Pierre Simon Laplace Climate Model (IPSLCM) (Dufresne et al. 2013) to study the effect of greening on key hydrological variables (precipitation, soil moisture, ET) in Australia. To study the climate impacts of greening under the modulation of ENSO, we employ three ocean SST states as boundary forcings in the ocean model: (1) climatology mean SST; (2) SST associated with strong El Niño (El Niño SST); and (3) SST associated with strong La Niña events (La Niña SST). This approach allows us to investigate the role of greening on modeled climate equilibria in a contained region hallmarked by observable LAI increases, and both brief wet periods and intensely dry periods. Details of the experiment are shown below in "Methods". By comparing the simulations with the same greening forcing but under three different SST patterns, we find three distinct equilibria of the regional climate. In the context of greening, the patterns under different SSTs conditions, the biosphere–atmosphere processes, and the underlying mechanisms will be discussed in the following content.

Methods

Model

The coupled land–atmospheric model used is the IPSLCM version 4 (Dufresne et al. 2013), which is involved in phase 5 of the Coupled Model Intercomparison Project (CMIP5) (Taylor et al. 2012). IPSLCM

contains the atmospheric component of the Laboratoire de Météorologie Dynamique zoom model (LMDZ) (Hourdin et al. 2006; Li 1999) and the land surface component of the Organizing Carbon and Hydrology in Dynamic Ecosystems (ORCHIDEE) (Krinner et al. 2005). In detail, ORCHIDEE contains a hydrological module SECHIBA (Ducoudré et al. 1993), a dynamic global vegetation model LPJ (Sitch et al. 2003), and a carbon module STOMATE consisting of terrestrial carbon dynamics and phenology (Krinner et al. 2005). Here only the SECHIBA is activated to calculate the energy and water exchange between the atmosphere and land and the soil water budget (Krinner et al. 2005). Vegetation distribution and LAI are prescribed using satellite observations in the model. The atmosphere component LMDZ is coupled with the surface component ORCHIDEE synchronously (Marti et al. 2005). The coupling process is performed via an interface model to couple the first atmospheric level variables (i.e., dry static energy, specific humidity, and wind speed) by the surface flux, which evolves over the vertical levels and time steps (Polcher et al. 1998). The atmosphere–biosphere coupled IPSLCM is shown to produce satisfactory simulations of surface sensible and latent fluxes (Krinner et al. 2005; Ngo-Duc et al. 2005). For the hydrological processes, the ORCHIDEE component includes the stream and two aquifer reservoirs: a fast reservoir for short-term water storage and a slow reservoir for long-term water storage (Marti et al. 2005). However, these reservoirs are not connected to the deep soil moisture and the groundwater simulation is absent in the model (Marti et al. 2005). River routing processes interact with surface processes through runoff and drainage, but the routing scheme in the model does not affect the land surface processes, which means there is no evaporation in the rivers (Marti et al. 2005). Despite the challenging tasks of simulating the water storage in the model, the simulated hydrological discharge in the model is verified to present rather good results compared with the observations (Hagemann and Dumenil 1997).

IPSLCM has been widely accepted in past efforts to study greening-involved land–atmospheric processes (Zeng et al. 2017, 2018a, b; Li et al. 2018; Lian et al. 2020). Importantly, IPSLCM is confirmed to be proficient in capturing the climate changes to the subtle perturbation of vegetation, which can be reflected by the metric of the ratio of plant transpiration (T) to total ET (T/ET) (Berg and Sheffield 2019). The T/ET value computed from the IPSLCM reaches 60%, which is near the value indicated as the realistic global T/ET (Good et al. 2015). Further, IPSLCM outperforms many other Earth System Models in capturing the changes in land–atmospheric processes when perturbing the vegetation (Berg and Sheffield 2019).

Experiment design

The simulations are performed following the Atmospheric Model Intercomparison Project (AMIP) framework by coupling the land and atmosphere components with the prescribed ocean. Prior to simulation, the model was spun up from a cold start and ran for 60 years to allow all diagnostic simulations to start with the same reasonable initial states. We use the LAI3g global LAI dataset to extract the evolution of greening patterns over time and space (Zhu et al. 2013). To integrate the satellite-derived LAI into the land component ORCHIDEE, we first interpolate the original LAI3g values (1/12 degree; 15 days) to match the $1.5^\circ \times 3.0^\circ$ resolution of other model inputs. According to the increasing trend of satellite-derived LAI during 1982–2011 (Additional file 1: Fig. S1), we then replaced the static LAI values with monthly satellite-derived LAI for two periods of 1982–1986 (1980s) and 2007–2011 (2010s) to represent low and high LAI conditions (Table 1). This time-varying LAI was applied for all model plant function types at the pixel level ($1.5^\circ \times 3.0^\circ$). We performed a suite of six diagnostic simulations that were based on the three SST states (see below) and the two time periods of satellite-derived LAI (Table 1). All simulations start with the same initial condition but with different forcing of LAI and SST, each running for another 60 years (Table 1). The results are presented as the 60-year average for each simulation. We prescribe greening in the model as the difference between the satellite-derived LAI during the 2010s and that during the 1980s (Fig. 1).

To consider the impacts of ENSO, three SST states are applied in the ocean model as boundary forcings (Table 1). The AMIP provides monthly maps of SST and sea ice data. The El Niño SST is derived from the monthly data averaged for those years when El Niño was moderate to strong (1982, 1986, 1987, 1991, 1994, 1997, 2002, and 2009); and the La Niña SST is averaged for moderate to strong La Niña years (1988, 1999, 2007, and 2010). The climatology mean SST was determined for the average of the whole period of 1982–2011. The baseline simulations used for comparison with wet and dry states are based on the climatology mean SST forcing.

Accordingly, there are three experiments designed from the six simulations (Table 1). The first experiment is derived by the difference between SIM2 and SIM1 (SIM2–SIM1) to identify the greening under climatology mean SST. SIM1 is forced by low LAI and climatology mean SST, and SIM2 is forced by high LAI and climatology mean SST. The second experiment (SIM4–SIM3) is designed to explore the greening under El Niño SST. SIM3 and SIM4 are forced by the same El Niño SST low (SIM3) and high (SIM4) LAI. The third experiment refers to the difference between SIM6 and SIM5 (SIM6–SIM5)

Table 1 Simulations and experiment design with different forcings of LAI and SSTs

Simulations	LAI	SST
SIM1	The 1980s	Climatology mean
SIM2	The 2010s	Climatology mean
SIM3	The 1980s	El Niño
SIM4	The 2010s	El Niño
SIM5	The 1980s	La Niña
SIM6	The 2010s	La Niña
Experiment design	**Formula**	**Purpose**
EXP1	SIM2-SIM1	Greening under climatology mean SST
EXP2	SIM4-SIM3	Greening under El Niño
EXP3	SIM6-SIM5	Greening under La Niña

The difference between SIM2 and SIM1 (SIM2–SIM1) is used to identify the greening under climatology mean SST. SIM4–SIM3 indicates the greening under El Niño and SIM6–SIM5 refers to greening under La Niña

aimed to study the greening under La Niña SST. SIM5 and SIM6 are forced by the same La Niña SST and the low and high LAI, respectively.

Validation

To validate the model results, we compared the modeled precipitation and ET with observation-based datasets. To validate the precipitation, we use the gridded ($0.5^\circ \times 0.5^\circ$) Climate Research Unit (CRU) Time-series (TS) version 4.05 dataset, provided by the University of East Anglia Climate Research Unit (CRU et al. 2021). To validate the ET, we used a global ET dataset with monthly values at 0.5° resolution provided by Jung et al. (2010). The ET data are derived by integrating the in situ measurements at the FLUXNET sites, satellite images of the fraction of photosynthetically active radiation absorbed by the canopy (FAPAR), and surface meteorological data (Jung et al. 2010). To compare with the model results, the observational-based precipitation and ET datasets are interpolated linearly to $1.5^\circ \times 3.0^\circ$ grids to match the model; and annual means were computed for land-dominated grid cells of the Australian continent.

A comparison of model results with these observational-based data indicates that the model is able to construct the climatology mean patterns of precipitation and ET, but the magnitude of precipitation and ET in the coastal regions is underestimated (Additional file 1: Figs. S2, S3). The underestimation is likely due to the model being forced by the climatology mean SST, thus the interannual variations are not considered. The model generally estimates dry and wet patterns under El Niño and La Niña, despite discrepancies occurring in the magnitude and patterns of precipitation and ET. The precipitation change under ENSO is overestimated, but mainly in central and western Australia (Additional file 1: Fig. S2). The ET change is also overestimated in the model simulations under ENSO (Additional file 1: Fig. S3). The discrepancies between the model results and the observed pattern may result because the model only couples the land component and the atmosphere component. Such an AMIP framework driven by the static SST and sea ice of the model may be unable to reproduce some of the complex ocean–atmospheric characteristics (Gates et al. 1999). Additionally, the ENSO-related impacts are likely to have a lag effect, thus the magnitude of observed precipitation and ET change may be delayed to reach its maximum after the ENSO active phases (Liguori et al. 2022).

Satellite-derived and reconstructed observational data

To discuss the climate variabilities in Australia from 1982 to 2011, we use observation-based datasets of LAI, precipitation, and SST. LAI is again constructed from the LAI3g dataset (see above). For monthly Australian mean precipitation data, we use the gridded ($0.5^\circ \times 0.5^\circ$) CRU TS version 4.05 dataset (CRU et al. 2021). The precipitation data required were interpolated to $1.5^\circ \times 3.0^\circ$ grids to match the model, and annual means were computed for land-dominated grid cells of the Australian continent. For SST, we use the $2^\circ \times 2^\circ$ gridded monthly NOAA Extended Reconstructed Sea Surface Temperature V3b dataset (Smith et al. 2008), which again was interpolated to match the model grid spacing. We also use this SST product to compute the Niño 3.4 index, which allows for examining the interactions between precipitation and ENSO.

Results

Relationship between SST and precipitation

Alternating spatially dry and wet patterns across Australia are associated with the different SST forcings used in the experiments. The simulated mean annual precipitation averaged over Australia using the climatology mean SST is 307.8 mm. The highest precipitation concentrates in the northern and eastern coastal regions, and especially in the southeastern area; precipitation is lowest in the arid and semi-arid central regions (Fig. 2a). For the La Niña SST simulations, Australia is wetter with an increased mean annual precipitation of 403.9 mm. Precipitation is higher for the baseline simulations using the mean climatology SST, particularly in the northwestern and southeastern regions (Fig. 2b). In contrast, simulated mean annual precipitation drops to 253.9 mm using the El Niño SST as forcing (Fig. 2c).

Multiple equilibria for the same greening

With the same forcing of greening integrated into the model, we found that three different equilibria are reached using the three different SST forcings (Fig. 2). Over the whole Australian continent, greening-induced changes of soil moisture were quite variable: + 0.9 mm under La Niña SST forcing; − 1.9 mm using the climatology mean SST forcing, and − 13.9 mm under El Niño SST (Additional file 1: Table S1). For the baseline case (climatology mean SST forcing), the soil moisture changes under greening are spatially heterogeneous (Fig. 3a). Soil moisture declines in the eastern coastal regions, but increases slightly in the western regions (Fig. 3a). In the regions where LAI change is small (< 10th percentile), the soil moisture change is negligible (− 0.4 ± 4.8 mm). Then as LAI increases, based on linear regression, soil moisture decreases 8.9 ± 1.6 mm per m^2 m^{-2} (Wald test $p < 0.01$; Fig. 3b).

For the wet La Niña condition, many regions of the continent experience a slight increase in soil moisture (Fig. 3c). The small decrease mainly occurs in the north or east, while the west generally experiences a slight increase. The heterogeneity of the soil moisture change is similar to the climatology mean SST case, but with a smaller magnitude. Overall, soil moisture significantly increases in the regions where LAI changes are slight (2.2 ± 1.2 mm, t-test $p < 0.01$). The association (again linear regression) between soil moisture and LAI is also less negative (− 6.1 ± 0.8 mm per m^2 m^{-2}; Wald test $p < 0.01$; Fig. 3d), implying that greening has a small effect on soil moisture during La Niña conditions when increases in both rainfall and ET are somewhat in balance.

For the drier condition associated with El Niño, soil moisture decreases profoundly in response to greening throughout the continent, with a few exceptions along the western coast (Fig. 3e). The linear association between soil moisture and LAI during the El Niño condition is − 8.1 ± 3.4 mm per m^2 m^{-2} ($R^2 = 0.03$, Wald test $p > 0.01$; Fig. 3f), which is similar to that under the climatology mean SST forcing (Fig. 3b). However, soil moisture depletion occurs in most regions, especially in the central, northern, and southeastern parts of the continent (Fig. 3e). Despite drying occurring throughout most of the continent, the association is spatially complex. In regions where LAI change is subtle, soil moisture decreases by 5.0 ± 14.4 mm (t-test $p > 0.01$). More than half of the grids with decreasing soil moisture occur simultaneously with the small increase in LAI (Fig. 3e)—resulting in the low R^2 of the regression (Fig. 3f).

Changes in water yield under greening

Water yield, which reflects the available water supply is defined as the difference between precipitation (P) and ET, denoted as P-ET (Brown et al. 2005; Ellison et al. 2011). Greening shapes water yield, in part, through the feedback involving ET and precipitation. Our simulations show that these processes are modulated by ocean SST forcings associated with the background of dry and wet conditions in Australia, as discussed in the following paragraphs for the three SST forcings considered. In Australia, the magnitude of runoff change is relatively smaller than ET and precipitation (Additional file 1: Table S1, Fig. S4).

Using climatology mean SST forcing, greening results in a small continental-wide decrease in soil moisture (− 1.86 mm) despite annual increases in both precipitation (+ 7.1 mm) and ET (+ 3.7 mm), as shown in Fig. 4a. Regionally, precipitation and ET increase in the northern, southeast and western parts of the country (Fig. 4b, c). These two variables decrease in the central-east and central-west areas. However, the change tends to be more intense for precipitation than ET. The result is heterogeneity in water yield throughout the country, with distinct and large increases occurring in the north and the south, and large declines occurring in the east-southeast region. In this case, the limited water availability likely constrains the soil moisture in the areas of the east-southeast region.

In the wetter condition associated with La Niña, ET increases by 15.5 mm per year, and the precipitation increases by 24.4 mm per year, resulting in relatively moist conditions compared with the climatology mean SSTs baseline simulations just mentioned (Fig. 5a). The change of ET and precipitation is relevant to the previous finding that moist condition enables the increase of ET, which adds more precipitable water into the atmosphere (Forzieri et al. 2017). Spatially, ET increases largely in the eastern coastal part of the country, consistent with

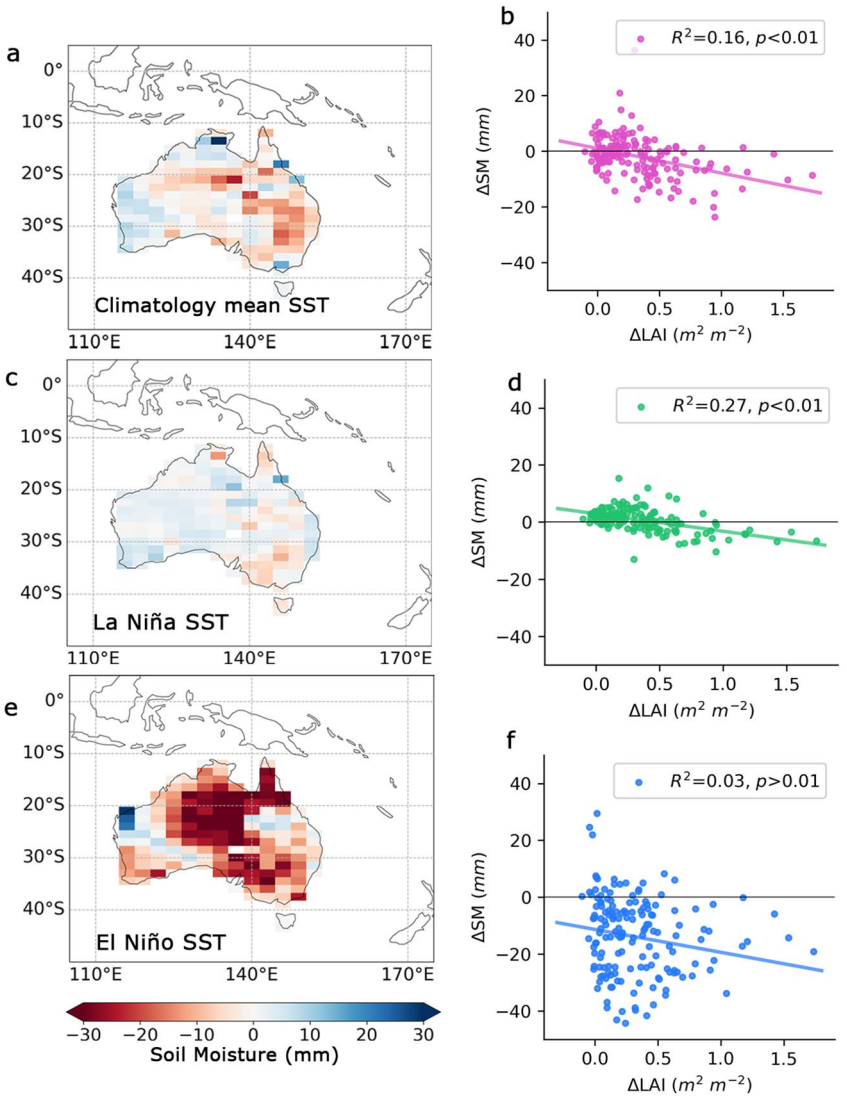

Fig. 3 The patterns of soil moisture in response to the greening under different sea surface temperatures (SSTs). Spatial patterns of changes in soil moisture under three SST model forcings: **a** climatology mean SST; **c** La Niña SST; and **e** El Niño SST. To test the relationships of spatial patterns between greening and the resulting soil moisture changes, sensitivity analysis through linear regression is applied. The sensitivity of soil moisture changes ΔSM to greening indicated by ΔLAI is computed as $\Delta SM = \theta \cdot \Delta LAI + c$, where the ΔSM and ΔLAI come from the spatial patterns including a total of 163 pixels within Australia for each variable. The results are presented as the corresponding scatter plots of **b**, **d**, **f** under the climatology mean SST, La Niña SST, and El Niño SST, respectively

the increase of transpiration by vegetation (Fig. 5b, Additional file 1: Fig. S5b). In these regions, the enhanced evaporative cooling is coincident with the reduction in sensible heat (Additional file 1: Fig. S6b). Meanwhile, precipitation increases almost over the whole continent (Fig. 5c). In explanation, the large increase in precipitation is offset by a relatively large increase in ET, producing little change in water yield over eastern regions (Fig. 5d), which is consistent with the small decline in soil moisture (discussed in the prior section). On the other hand, the water yield is relatively greater in the northwestern part of the continent (Fig. 5d), suggesting that the water is sufficient to replenish soil moisture. Mainly due to the greater water yield, an increase in runoff occurs in the northwestern region (Additional file 1: Fig. S4b).

For the dry condition associated with El Niño, mean soil moisture decreases by 13.9 mm across the country (Fig. 6a). Continental declines are simulated for both ET (− 7.0 mm/year) and precipitation (− 9.8 mm/year). The

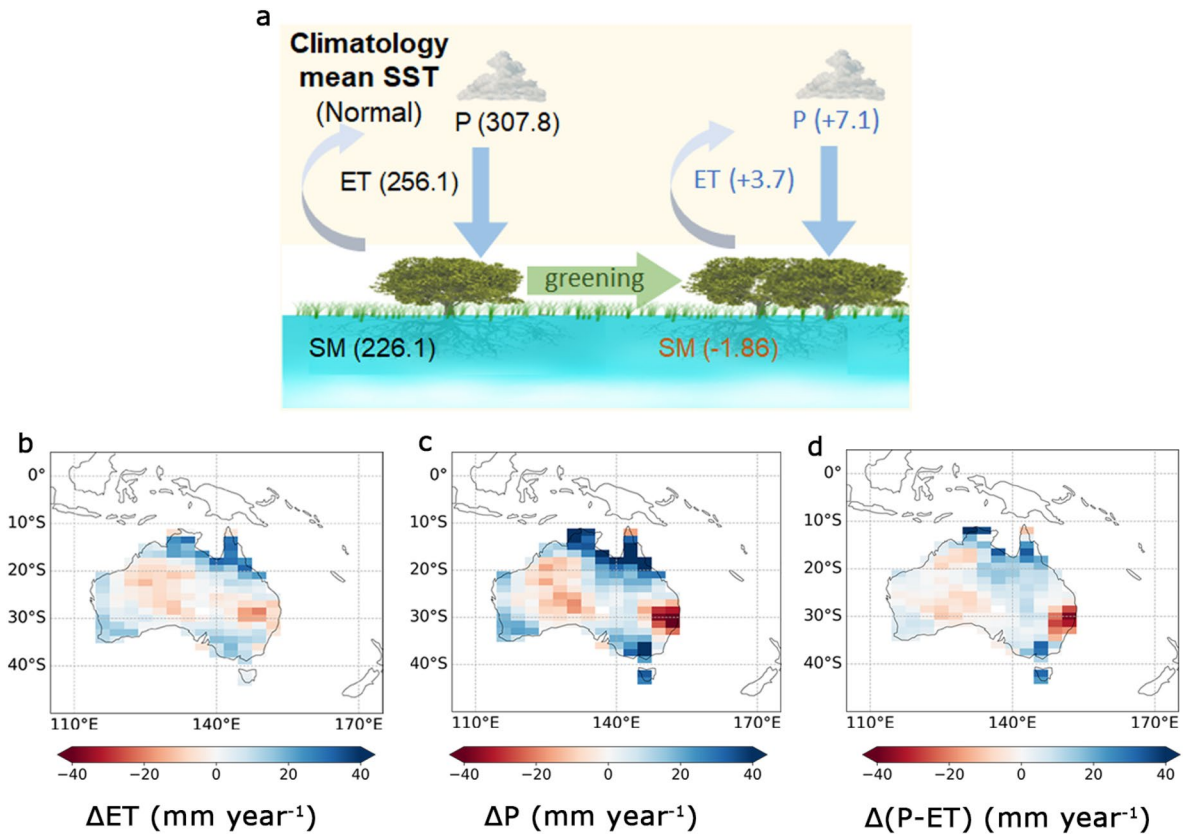

Fig. 4 Conceptual illustration and the spatial patterns of the modeled changes in water yield under greening for mean SST forcing. **a** The biosphere–atmosphere iterations before and after greening for hydrological balance variables ET (mm year^{-1}), precipitation (P, mm year^{-1}), and soil moisture (SM, mm). Flux is illustrated by upward (downward) arrows. The blue values indicate the increase (decrease) amount of the flux. The numbers represent changes in the variables. **b**–**d** The spatial patterns of the changes in ET, P, and water yield (P-ET) under greening

decreases in both ET and precipitation promote a decline in water yield in the northern, northwestern and southeastern regions (Fig. 6d). Under El Niño SST forcing, LAI increases associated with greening intensify water stress. The decrease in ET is mainly due to the decrease in soil evaporation (Additional file 1: Fig. S7c). The evaporation is limited by the available water in Australia (Deng et al. 2020). Under greening, the evaporation is further depressed over the whole region, reflecting intensified water stress (Additional file 1: Fig. S7c). Though the transpiration shows an increase mainly in the eastern coastal region due to greening, such an increase is much smaller compared with the climatology mean and La Niña SST forcing conditions, suggesting that the available water for transpiration is reduced (Additional file 1: Fig. S5). The resulting large depletion of soil moisture is likely because soil moisture is not sufficiently supplemented but, rather, is consumed by ET over the simulation period (Additional file 1: Fig. S8b). As model results are averaged over time, the soil moisture pattern reflects a substantial reduction. Moreover, the suppressed ET could partially decrease the precipitation as less moisture recycling occurs, thereby exacerbating the dry conditions and contributing to soil moisture depletion (Schumacher et al. 2022).

Large-scale moisture transport influenced by greening

Given that the change in precipitation is larger than the corresponding change in ET, the large-scale moisture circulation pattern is disturbed as a result of greening (Shukla et al. 1990). Here we further explore relevant patterns of the large-scale atmospheric circulation in the model (Fig. 7a–c). In the general case (climatology mean SST simulation), the atmosphere is rich in water vapor in tropical northern Australia as moisture is transported from the western Pacific. Moisture in the southernmost regions is transported from the Indian Ocean and Southern Oceans, but the contribution to precipitable water is weak in these regions (Fig. 7a–c). These modeled patterns of the large-scale atmospheric circulation are consistent with observations that much precipitation originated

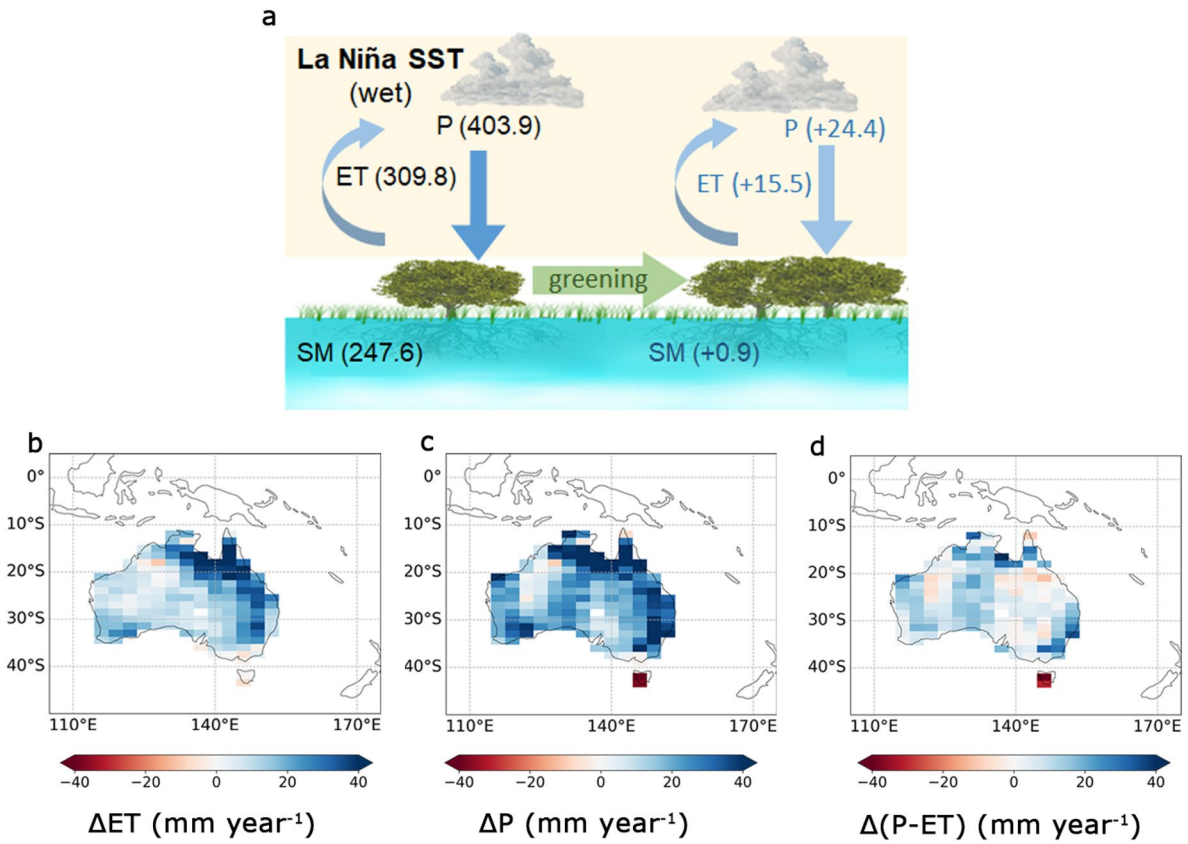

Fig. 5 Conceptual illustration and the spatial patterns of the modeled changes in water yield under greening for La Niña SST forcing. **a** The biosphere–atmosphere iterations before and after greening for hydrological balance variables ET (mm year^{-1}), precipitation (P, mm year^{-1}), and soil moisture (SM, mm). **b**–**d** The spatial patterns of the changes in ET, precipitation (P), and water yield (P-ET) under greening

from the tropical Pacific and Tasman Sea (Holgate et al. 2020).

In contrast, simulated precipitation patterns associated with wet (La Niña SST) and dry (El Niño SST) conditions in Australia are attributed to the anomalous advection patterns that result from the different SST forcings considered. For the La Niña SST forcing, increased precipitable water originates from moisture transported from the tropical oceans (Additional file 1: Fig. S9). For the El Niño SST forcing, the atmosphere is drier because the moisture from the tropical Pacific Ocean is suppressed, reducing the precipitable water in northwestern Australia in particular. Water vapor in this case is mainly transported from the Indian Ocean and Southern Oceans. Consequently, the inland regions of the continent, which are mostly arid and semi-arid, get even less atmospheric moisture supplemented from the ocean (Additional file 1: Fig. S9). Our simulations show that the changes induced by greening on large-scale circulations in Australia are discernable versus the pre-greening situation (compare Fig. 7d–f with Fig. 7a–c), in line with the effect of a previous study (Li et al. 2018). The changes in moisture transport are the product of the remote influence of land-based greening on circulation patterns (Li et al. 2018; Schumacher et al. 2022; van der Ent et al. 2010). For example, under the climatology mean SST, moisture is transported from the tropical Indian Ocean into the northern land areas, contributing to the increase in precipitation, compared with the case prior to greening (Figs. 4b, 7a vs. 7d). The increase of LAI produces a small decrease of albedo (Additional file 1: Fig. S10), yet the reduction of downward shortwave radiation at the surface in the northern and southern coastal regions implies the convergence of moisture (Additional file 1: Fig. S10; Li et al. 2018). Meanwhile, the depletion of precipitable water in the central-east region can be attributed to a greening-induced divergence of moisture, which is implied by the increase of downward shortwave radiation (Fig. 7a, d; Additional file 1: Fig. S10). As a result, precipitation is likely to be further restricted (Fig. 4b).

Under La Niña SST forcing, greening amplifies wetness as atmospheric water vapor increases over the whole continent (Fig. 7e). Enhanced moisture is transported from the Indian Ocean inland (Fig. 7e) where it tends to

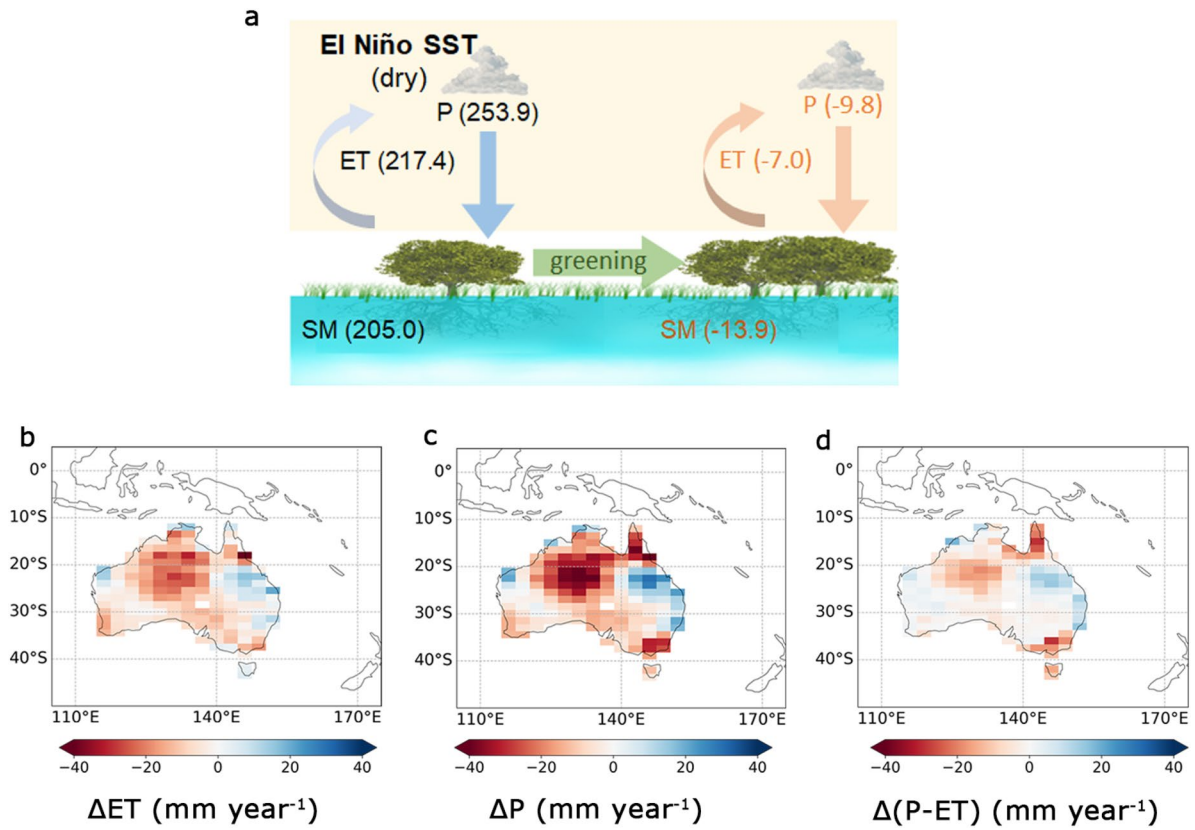

Fig. 6 Conceptual illustration and the spatial patterns of the modeled changes in water yield under greening for El Niño SST forcing. **a** The biosphere–atmosphere iterations before and after greening for hydrological balance variables ET (mm year^{-1}), precipitation (P, mm year^{-1}), and soil moisture (SM, mm). **b**–**d** The spatial patterns of the changes in ET, precipitation (P), and water yield (P-ET) under greening

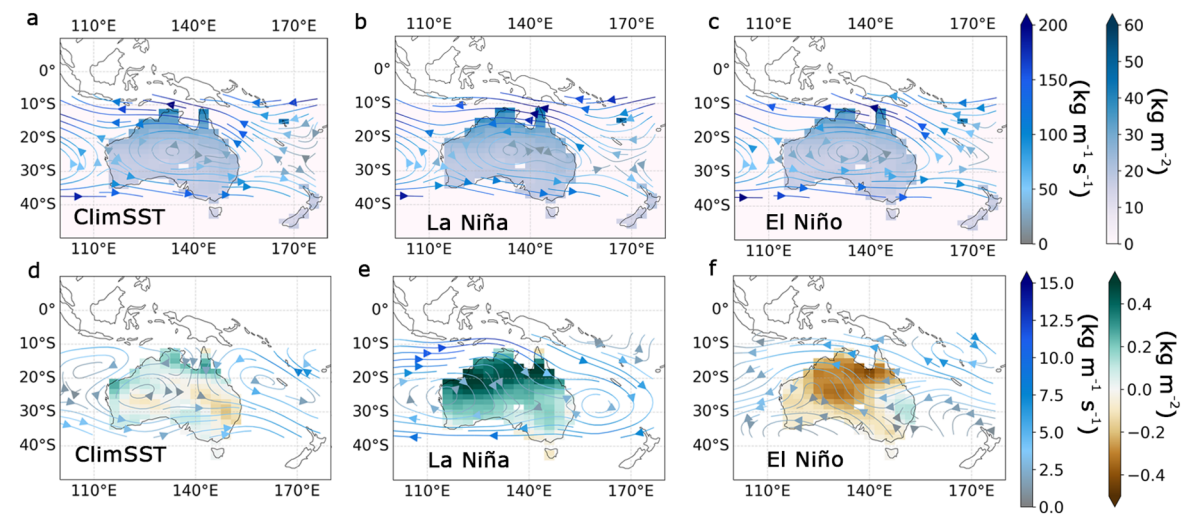

Fig. 7 Moisture transport (primary axis) and precipitable water (secondary axis) before (top row) and after the greening (bottom row). The top row shows the patterns of moisture transport (contour) and precipitable water (shading) prior to greening for the three simulation SST forcings: **a** climatological mean SST; **b** La Niña SST; and **c** El Niño SST. The magnitude of moisture transport is calculated as u and v components of moisture flux ($\sqrt{u^2+v^2}$). The bottom row of figures shows the changes in moisture transport and precipitable water under greening for the same three simulation SST forcings: **d** climatological mean SST; **e** La Niña SST; and **f** El Niño SST. The arrows indicate the changes in moisture transport, for which the magnitude is calculated as the changes of u and v components of moisture flux ($\sqrt{\Delta u^2+\Delta v^2}$)

converge, as reflected by the reduction of surface shortwave downward radiation (Additional file 1: Fig. S11). The enhanced moisture transport is likely to increase precipitation, which may increase soil moisture. Further, ET is less constrained by soil moisture content in these wetter conditions—a result that is in line with accelerated moisture recycling that has been shown to be associated with greening (Zeng et al. 2018a, b).

Under El Niño SST forcing, greening exacerbates dryness by decreasing precipitable water throughout much of the continent (compare Fig. 7c versus 7f). The divergence of moisture in the west hinders the moisture transported from the tropical Pacific Ocean into the interior of the continent where the greatest desiccation occurs (Fig. 7f; Additional file 1: Fig. S10). The deficit of atmospheric moisture and reduced ET for dryer soil conditions contribute to the profound decrease of precipitation in the north and northwest regions (Figs. 6b, c 7c, f). Meanwhile, the increasing moisture near the Tasman Sea and the local greening-enhanced ET partially alleviate dry conditions in the eastern coastal region (Fig. 7f). Nevertheless, greening-intensified drying tends to exacerbate the soil moisture depletion throughout most of the continent under El Niño SST forcing (Fig. 3d).

Discussion

The interpretation of our results may need caution due to the limitations of the experiment design. We prescribed the El Niño and La Niña SSTs by averaging data from past ENSO events. This approach neglects certain characteristics of the time-evolving ENSO. For example, an ENSO event is likely to have a lag effect, meaning the ENSO impact on precipitation and ET may be delayed from the active ENSO phase (Liguori et al. 2022). Moreover, ENSO events have intrinsic asymmetry. For example, El Niño generally has greater amplitudes and produces stronger impacts than La Niña events (An and Jin 2004). Thus, the model driven by the observed ENSO SSTs patterns may reinforce this asymmetry (An and Jin 2004). Also, our simulation does not elucidate other climate modes affecting Australia, such as the Indian Ocean Dipole and the Southern Annular Mode (McIntosh et al. 2009). These climate phenomena can either influence Australian weather and ecosystems individually or they may be superposed onto the responses to ENSO events (Wang and Cai 2020). In addition, the model configuration in this study does not consider the carbon and vegetation dynamics, future analyses are also expected to replenish the results on carbon fluxes.

Additional to the soil moisture change, the change in terrestrial water storage may need more attention when evaluating the climate impacts of greening. The current absence of groundwater and terrestrial water storage simulation in the model may affect the results. For example, soil moisture can be resupplied in some topographic locations by a number of processes (capillary rise, subsurface flow, return flow) that facilitate ET even in periods of low rainfall (Wang et al. 2016). Moreover, in agricultural areas such as southeastern Australia, irrigation may intensify the evaporative cooling effects and modulate the interannual precipitation patterns (Mahmood et al. 2014). Improvements in models are expected to reproduce more realistic processes.

Despite these limitations, the modeling results may also provide insight into understanding the surface conditions in Australia and the climatic precursors of wildfires. The observed variations of wet and dry conditions are correlated with the ENSO cycle (Fig. 8). Enhanced vegetation under wet conditions tends to increase ET and reduce soil moisture. We could then anticipate that the soil moisture is resupplied by the increased precipitation, forming a delicate equilibrium. As the wet condition suddenly shifts to the dry condition, such as during an El Niño event, the enhanced vegetation is not likely to perish simultaneously, but endures for a period of time (Wang and Eltahir 1999). Accordingly, system feedbacks during dry periods and greening tend to deplete soil moisture, eventually leading to defoliation, which can act as the fuel for wildfires (Abram et al. 2021). Therefore, understanding the different climate impacts associated with greening for wet and dry states may contribute to a greater ability to predict and manage wildfires. For example, the 2019–2020 wildfires in Australia coincided with dry conditions of combined El Niño and positive Indian Ocean Dipole (Wang and Cai 2020), but the prior year was characterized by relatively wet La Niña conditions which were favorable for the growth of living forage. Vegetation-based mitigation policies to combat global warming may need to exercise caution in semi-arid regions to avoid adverse effects.

Conclusion

Our simulations show that distinct climate equilibria occur in Australia as a result of the interaction of greening and ENSO-associated SST states. In the climatology mean SST simulations, greening brings about a reduction in soil moisture, and increases in precipitation and ET, but the spatial patterns of these changes are highly heterogeneous across the continent. In contrast, greening tends to increase soil moisture during the wet conditions of La Niña by enhancing moisture recycling. However, in dry conditions of El Niño, greening intensifies the water stress and largely depletes the soil moisture. Distinct modes of climate as results of greening appear in both water availability and moisture transport. These distinct modes spanning dry and wet

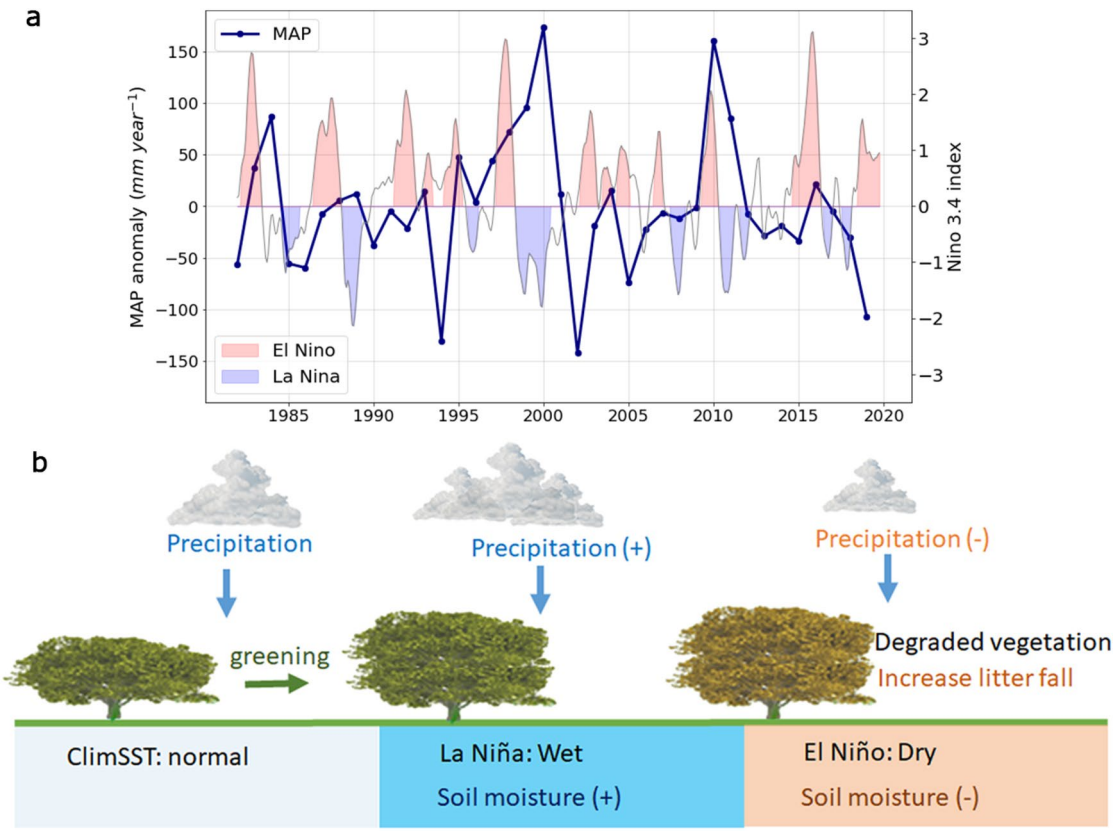

Fig. 8 The temporal variation of mean annual precipitation (MAP) anomaly for ENSO conditions. **a** The temporal variations of MAP anomaly were calculated as the MAP extracted from the means for the whole period of 1982–2020. The Niño3.4 index is used to identify the El Niño events (red shading) and La Niña events (blue shading). **b** The conceptual figure illustrates the changes in surface conditions associated with the alternating wet and dry climate variability contributed by the different SST forcing

climates in semi-arid land are largely attributed to differences in large-scale ocean–atmospheric circulation and different climate feedbacks.

In our previous study, the climate effects of greening in Australia were divergent between two numerical experiments using either observed variable SST or climatological mean SST as forcing (Zeng et al. 2017). When SSTs were updated year by year, the greening was found to lead to a cooler and wetter climate in Australia; however, when SST was fixed as the climatology mean, the simulated climate effect of the greening reversed and caused a warmer and drier climate (Zeng et al. 2017). The observed divergence can be explained by the finding in this study: increasing La Niña years during past decades will trigger greening-induced wetter and cooler conditions, and vice versa for El Niño. A similar mechanism associated with the interplay of greening and SST variation may also work for the different climate impacts of greening in other hotspots, necessitating more in-depth investigations.

Abbreviations

SST: Sea surface temperatures; LAI: Leaf Area Index; ET: Evapotranspiration; ENSO: El Niño and Southern Oscillation; IPSLCM: Institute Pierre Simon Laplace Climate Model; LMDZ: Laboratoire de Météorologie Dynamique zoom model; ORCHIDEE: Organizing Carbon and Hydrology in Dynamic Ecosystems; T: Transpiration; T/ET: The ratio of plant transpiration to total evapotranspiration.

Supplementary Information

The online version contains supplementary material available at https://doi.org/10.1186/s40562-022-00252-9.

Additional file 1. Additional figures and tables.

Acknowledgements

Z.Z. sincerely thanks the AOGS invitation to present a Kamide Lecture and publish this Kamide Lecture paper. We thank Profs. Ji Chen, Young-Oh Kim, Robin Robertson and the three anonymous referees for providing insightful comments on this study.

Author contributions

ZZ designed the research and performed the numerical simulations; SL performed the analysis and wrote the draft. All authors contributed to the interpretation of the results and the writing of the paper. All authors read and approved the final manuscript.

Funding
This study was supported by the National Natural Science Foundation of China (Grants nos. 42071022, 42001321) and the start-up fund provided by Southern University of Science and Technology (no. 29/Y01296122).

Availability of data and materials
The monthly maps of sea surface temperature and sea ice data to drive the model can be found in the Atmospheric Model Intercomparison Project (AMIP; https://pcmdi.llnl.gov/mips/amip/amip.html). The NOAA Extended Reconstructed Sea Surface Temperature V3b dataset is obtained from https://psl.noaa.gov/data/gridded/data.noaa.ersst.v3.html. The CRU TS version 4.05 is available at https://catalogue.ceda.ac.uk/uuid/edf8febfdaad48abb2cbaf7d7e846a86.

Declarations

Competing interests
The authors declare no competing interests.

Author details
[1]School of Environmental Science and Engineering, Southern University of Science and Technology, Shenzhen, China. [2]Faculty of Fisheries Technology and Aquatic Resources, Maejo University, Chiang Mai, Thailand. [3]Laboratoire de Météorologie Dynamique, Centre National de la Recherche Scientifique, Sorbonne Université, Ecole Normale Supérieure, Ecole Polytechnique, Paris, France. [4]Department of Geoscience and Natural Resource Management, University of Copenhagen, Copenhagen, Denmark.

Received: 8 August 2022 Accepted: 29 October 2022
Published online: 11 November 2022

References

Abram NJ et al (2021) Connections of climate change and variability to large and extreme forest fires in southeast Australia. Commun Earth Environ. https://doi.org/10.1038/s43247-020-00065-8
An S, Jin F (2004) Nonlinearity and asymmetry of ENSO. J Clim 17(12):2399–2412. https://doi.org/10.1175/1520-0442(2004)017%3c2399:NAAOE%3e2.0.CO;2
Berg A, Sheffield J (2019) Evapotranspiration partitioning in CMIP5 models: uncertainties and future projections. J Clim 32(10):2653–2671. https://doi.org/10.1175/jcli-d-18-0583.1
Brown AE, Zhang L, McMahon TA, Western AW, Vertessy RA (2005) A review of paired catchment studies for determining changes in water yield resulting from alternations in vegetation. J Hydrol 310(1–4):28–61. https://doi.org/10.1016/j.jhydrol.2004.12.010
Chen C, Eamus D, Cleverly J, Boulain N, Cook P, Zhang L, Cheng L, Yu Q (2014) Modelling vegetation water-use and groundwater recharge as affected by climate variability in an arid-zone Acacia savanna woodland. J Hydrol 519:1084–1096. https://doi.org/10.1016/j.jhydrol.2014.08.032
Chen C et al (2019) China and India lead in greening of the world through land-use management. Nat Sustain 2:122–129. https://doi.org/10.1038/s41893-019-0220-7
Chen C, Li D, Li Y, Piao S, Wang X, Huang M, Gentine P, Nemani RR, Myneni RB (2020) Biophysical impacts of Earth greening largely controlled by aerodynamic resistance. Sci Adv 6:eabb1981
Deng Y, Wang S, Bai X, Luo G, Wu L, Chen F, Wang J, Li C, Yang Y, Hu Z, Tian S, Lu Q (2020) Vegetation greening intensified soil drying in some semi-arid and arid areas of the world. Agric For Meteorol. https://doi.org/10.1016/j.agrformet.2020.108103
Donohue RJ, McVicar TR, Roderick ML (2009) Climate-related trends in Australian vegetation cover as inferred from satellite observations, 1981–2006. Glob Chang Biol 15(4):1025–1039
Ducoudré NI, Laval K, Perrier A (1993) SECHIBA, a new set of parameterizations of the hydrologic changes at the land-atmosphere interface within the LMD atmospheric general circulation model. J Clim 6:248–273
Dufresne JL et al (2013) Climate change projections using the IPSL-CM5 Earth System Model: from CMIP3 to CMIP5. Clim Dyn 40:2123–2165. https://doi.org/10.1007/s00382-012-1636-1
Ellis TW, Hatton TJ (2008) Relating leaf area index of natural eucalypt vegetation to climate variables in southern Australia. Agric Water Manag 95(6):743–747. https://doi.org/10.1016/j.agwat.2008.02.007
Ellison D, Futter MN, Bishop K (2011) On the forest cover-water yield debate: from demand- to supply-side thinking. Glob Change Biol 18(3):806–820. https://doi.org/10.1111/j.1365-2486.2011.02589.x
Feng X et al (2021) Recent leveling off of vegetation greenness and primary production reveals the increasing soil water limitations on the greening earth. Sci Bull 66(14):1462–1471. https://doi.org/10.1016/j.scib.2021.02.023
Forzieri G, Alkama R, Miralles DG, Cescatti A (2017) Satellites reveal contrasting responses of regional climate to the widespread greening of earth. Science 356:1180–1184
Gates WL et al (1999) An overview of the results of the Atmospheric Model Intercomparison Project (AMIP I). Bull Am Meterol Soc 73:1962–1970
Good SP, Noone D, Bowen G (2015) Hydrologic connectivity constrains partitioning of global terrestrial water fluxes. Science 349:175–176
Hagemann S, Dümenil L (1997) A parametrization of the lateral waterflow for the global scale. Clim Dyn 14:17–31. https://doi.org/10.1007/s003820050205
Hill MJ, Senarath U, Lee A, Zeppel M, Nightingale JM, Williams RJ, McVicar TR (2006) Assessment of the MODIS LAI product for Australian ecosystems. Remote Sens Environ 101(4):495–518. https://doi.org/10.1016/j.rse.2006.01.010
Holgate CM, Evans JP, van Dijk AIJM, Pitman AJ, Di Virgilio G (2020) Australian precipitation recycling and evaporative source regions. J Clim 33(20):8721–8735. https://doi.org/10.1175/jcli-d-19-0926.1
Hourdin F et al (2006) The LMDZ4 general circulation model: climate performance and sensitivity to parametrized physics with emphasis on tropical convection. Clim Dyn 27(7–8):787–813. https://doi.org/10.1007/s00382-006-0158-0
Hutley LB, O'Grady AP, Eamus D (2001) Monsoonal influences on evapotranspiration of savanna vegetation of northern Australia. Oecologia 126(3):434–443. https://doi.org/10.1007/s004420000539
Jiao T, Williams CA, De Kauwe MG, Schwalm CR, Medlyn BE (2021) Patterns of post-drought recovery are strongly influenced by drought duration, frequency, post-drought wetness, and bioclimatic setting. Glob Chang Biol 27(19):4630–4643. https://doi.org/10.1111/gcb.15788
Jung M et al (2010) Recent decline in the global land evapotranspiration trend due to limited moisture supply. Nature 467:951–954
Krinner G, Viovy N, de Noblet-Ducoudré N, Ogée J, Polcher J, Friedlingstein P, Ciais P, Sitch S, Prentice IC (2005) A dynamic global vegetation model for studies of the coupled atmosphere-biosphere system. Glob Biogeochem Cycles. https://doi.org/10.1029/2003gb002199
Li Z-X (1999) Ensemble atmospheric GCM simulation of climate interannual variability from 1979 to 1994. J Clim 12(4):986–1001
Li Y et al (2018) Divergent hydrological response to large-scale afforestation and vegetation greening in China. Sci Adv 4:eear4182
Lian X et al (2020) Summer soil drying exacerbated by earlier spring greening of northern vegetation. Sci Adv 6:eaax0255
Liguori G, McGregor S, Singh M, Arblaster J, Di Lorenzo E (2022) Revisiting ENSO and IOD contributions to Australian precipitation. Geophys Res Lett. https://doi.org/10.1029/2021gl094295
Liu S, Liu R, Liu Y (2010) Spatial and temporal variation of global LAI during 1981–2006. J Geogr 20(3):323–332. https://doi.org/10.1007/s11442-010-0323-6
Mahmood R et al (2014) Land cover changes and their biogeophysical effects on climate. Int J Climatol 34(4):929–953. https://doi.org/10.1002/joc.3736
Marti O et al (2005) The new IPSL climate system model: IPSL-CM4, Technical note, IPSL. https://hal.archives-ouvertes.fr/hal-03319443/document
McIntosh PC, Pook MJ, Risbey JS, Wheeler MC, Hendon HH (2009) On the remote drivers of rainfall variability in Australia. Mon Weather Rev 137(10):3233–3253. https://doi.org/10.1175/2009mwr2861.1
Ngo-Duc T, Polcher J, Laval K (2005) A 53-year forcing data set for land surface models. J Geophys Res Atmos 110:D06116. https://doi.org/10.1029/2004JD005434
Notaro M, Chen G, Yu Y, Wang F, Tawfik A (2017) Regional climate modeling of vegetation feedbacks on the Asian-Australian monsoon systems. J Clim 30(5):1553–1582. https://doi.org/10.1175/jcli-d-16-0669.1
Piao S, Wang X, Park T, Chen C, Lian X, He Y, Bjerke JW, Chen A, Ciais P, Tømmervik H, Nemani RR, Myneni RB (2020) Characteristics, drivers and feedbacks

of global greening. Nat Rev Earth Environ 1(1):14–27. https://doi.org/10.1038/s43017-019-0001-x
Polcher J et al (1998) A proposal for a general interface between land surface schemes and general circulation models. Glob Planet Change 19:261–276
Poulter B et al (2014) Contribution of semi-arid ecosystems to interannual variability of the global carbon cycle. Nature 509:600–603
Risbey JS, Raupach MR, Pook MJ, Meyers GA, McIntosh PC, England MH, Briggs PR, Sen Gupta A, Ummenhofer CC (2011) Indian and Pacific Ocean influences on southeast Australian drought and soil moisture. J Clim 24(5):1313–1336. https://doi.org/10.1175/2010jcli3475.1
Schumacher DL, Keune J, Dirmeyer P, Miralles DG (2022) Drought self-propagation in drylands due to land-atmosphere feedbacks. Nat Geosci 15(4):262–268. https://doi.org/10.1038/s41561-022-00912-7
Shukla J, Nobre C, Sellers P (1990) Amazon deforest and climate change. Science 247:1322–1325
Sitch S et al (2003) Evaluation of ecosystem dynamics, plant geography and terrestrial carbon cycling in the LPJ dynamic vegetation model. Glob Change Biol 9:161–185
Smith TM, Reynolds RW, Peterson TC, Lawrimore J (2008) Improvements NOAAs historical merged land-ocean surface temperature analysis (1880–2006). J Clim 21:2283–2296
Spracklen DV, Arnold SR, Taylor CM (2012) Observations of increased tropical rainfall preceded by air passage over forests. Nature 489(7415):282–285. https://doi.org/10.1038/nature11390
Taylor KE, Stouffer RJ, Meehl GA (2012) An overview of CMIP5 and the experiment design. Bull Am Meteorol Soc 93(4):485–498. https://doi.org/10.1175/bams-d-11-00094.1
Thompson AJ, Zhu J, Poulsen CJ, Tierney JE, Skinner CB (2022) Northern Hemisphere vegetation change drives a Holocene thermal maximum. Sci Adv 8(15):eabj6535
Trenberth KE (1999) Atmospheric moisture recycling: role of advection and local evaporation. J Clim 12:1368–1381. https://doi.org/10.1175/1520-0442(1999)012%3c1368:AMRROA%3e2.0.CO;2
University of East Anglia Climatic Research Unit (CRU), Harris IC, Jones PD, Osborn T (2021) CRU TS4.05: Climatic Research Unit Time-Series (TS) version 4.05 of high-resolution gridded data of month-by-month variation in climate (Jan. 1901–Dec. 2020). NERC EDS Centre for Environmental Data Analysis. https://catalogue.ceda.ac.uk/uuid/c26a65020a5e4b80b20018f148556681
van der Ent RJ, Savenije HHG, Schaefli B, Steele-Dunne SC (2010) Origin and fate of atmospheric moisture over continents. Water Resour. https://doi.org/10.1029/2010wr009127
Wang G, Cai W (2020) Two-year consecutive concurrences of positive Indian Ocean Dipole and Central Pacific El Niño preconditioned the 2019/2020 Australian "black summer" bushfires. Geosci Lett. https://doi.org/10.1186/s40562-020-00168-2
Wang G, Eltahir EAB (1999) Biosphere-atmosphere interactions over West Africa II: multiple climate equilibria. Q J R Meterorol Soc 126(565):1239–1260
Wang X, Huo Z, Feng S, Guo P, Guan H (2016) Estimating groundwater evapotranspiration from irrigated cropland incorporating root zone soil texture and moisture dynamics. J Hydrol 543:501–509. https://doi.org/10.1016/j.jhydrol.2016.10.027
Winkler AJ et al (2021) Slowdown of the greening trend in natural vegetation with further rise in atmospheric CO_2. Biogeosciences 18(17):4985–5010
Wu J, Wang D, Li LZX, Zeng Z (2022) Hydrological feedback from projected earth greening in the 21st century. Sustain Horizons. https://doi.org/10.1016/j.horiz.2022.100007
Yu Y, Notaro M, Wang F, Mao J, Shi X, Wei Y (2017) Observed positive vegetation-rainfall feedbacks in the Sahel dominated by a moisture recycling mechanism. Nat Commun 8(1):1873. https://doi.org/10.1038/s41467-017-02021-1
Zeng Z et al (2017) Climate mitigation from vegetation biophysical feedbacks during the past three decades. Nat Clim Chang 7(6):432–436. https://doi.org/10.1038/nclimate3299
Zeng Z, Piao S, Li LZX, Wang T, Ciais P, Lian X, Yang Y, Mao J, Shi X, Myneni RB (2018a) Impact of earth greening on the terrestrial water cycle. J Clim 31(7):2633–2650. https://doi.org/10.1175/jcli-d-17-0236.1
Zeng Z, Peng L, Piao S (2018b) Response of terrestrial evapotranspiration to Earth's greening. Curr Opin Environ Sustain 33:9–25. https://doi.org/10.1016/j.cosust.2018.03.001
Zhu Z, Bi J, Pan Y, Ganguly S, Anav A, Xu L, Samanta A, Piao S, Nemani R, Myneni R (2013) Global data sets of vegetation Leaf Area Index (LAI)3g and Fraction of Photosynthetically Active Radiation (FPAR)3g derived from Global Inventory Modeling and Mapping Studies (GIMMS) Normalized Difference Vegetation Index (NDVI3g) for the Period 1981 to 2011. Remote Sens 5(2):927–948. https://doi.org/10.3390/rs5020927
Zhu Z et al (2016) Greening of the Earth and its drivers. Nat Clim Chang 6(8):791–795. https://doi.org/10.1038/nclimate3004

Publisher's Note